The Deformation Behavior Analysis and Mechanical Modeling of Step/Intercritical Quenching and Partitioning-Treated Multiphase Steels

HONGSHAN ZHAO, WEI LI, LI WANG, SHU ZHOU, and XUEJUN JIN

Two types of multiphase steels containing blocky or fine martensite have been used to study the phase interaction and the TRIP effect. These steels were obtained by step-quenching and partitioning (S-QP820) or intercritical-quenching and partitioning (I-QP800 & I-QP820). The retained austenite (RA) in S-QP820 specimen containing blocky martensite transformed too early to prevent the local failure at high strain due to the local strain concentration. In contrast, plentiful RA in I-QP800 specimen containing finely dispersed martensite transformed uniformly at high strain, which led to optimized strength and elongation. By applying a coordinate conversion method to the microhardness test, the load partitioning between ferrite and partitioned martensite was proved to follow the linear mixture law. The mechanical behavior of multiphase S-QP820 steel can be modeled based on the Mecking–Kocks theory, Bouquerel's spherical assumption, and Gladman-type mixture law. Finally, the transformation-induced martensite hardening effect has been studied on a bake-hardened specimen.

I. INTRODUCTION

MULTIPHASE design is an important strategy in developing new advanced high-strength steels (AHSS) that possess excellent strength and elongation.[1–3] A new heat treatment process termed quenching and partitioning (Q&P) has been proposed in the past for the development of multiphase AHSS steels with retained austenite (RA).[4] RA is stabilized by the depletion of carbon in the supersaturated martensite during the partitioning treatment.[5,6] In order to utilize the synergy between hard and soft phases, a final microstructure should have a matrix composed of ferrite and martensite with certain amount of RA after the steel is reheated to the intercritical temperature.[7] The overall deformation behavior will largely depend on the complex phase interaction between matrix phases and transformation-induced plasticity (TRIP) effect.

Regarding the study of dual-phase steels, the selection criterion for different mechanical models relies on the phase interaction between ferrite and martensite, which affects the stress/strain partitioning[8] during deformation.[9–11] The issues of interest are whether the plastic deformation of martensite takes place,[12,13] and if so how the two phases deform relative to each other if the martensite yields.[14–16] The deformation behavior of martensite is said to be mainly dependent on its yield strength, the morphology, and distribution. These factors are determined by carbon content, which may change with martensite volume fraction[17] or the temper treatment,[18] the initial microstructure, and corresponding heat treatment.[11,19]

As to the TRIP effect, the mechanical property enhancement may be related to the local strengthening of the matrix by the elastic accommodation of the transformation[20] or the second-phase hardening by the existence of continuous appearance of martensite.[21–23] Matrix near the transformation-induced martensite particles can be significantly strengthened by the increased dislocation density.[24] If RA located in/near the local softened region transforms timely, the matrix can deform continuously without local failure. However, RA transformation out of synchronization with the deformation does little improvement to the mechanical properties. On the other hand, the existence of martensite particles results in larger extent of work hardening,[25,26] and subsequently improves the strength according to the induced martensite volume fraction.[3,23] Although different models have been applied to analyzing the TRIP effect, it is a research topic that still awaits further clarification.

In this study, two types of Q&P-treated multiphase steels with different morphologies and distributions of martensite have been used to analyze the phase interaction between matrix phases and the TRIP effect. A variety of characterization techniques were used to reveal the strain distribution and dislocation evolution

HONGSHAN ZHAO, Ph.D. Student, and XUEJUN JIN, Professor, are with the State Key Lab of Metal Matrix Composites, School of Materials Science and Engineering, Shanghai Jiao Tong University, Shanghai 200240, China, and also with the Collaborative Innovation Center for Advanced Ship and Deep-Sea Exploration, Shanghai 200240, China. Contact e-mail: jin@sjtu.edu.cn WEI LI, Lecturer, is with the Institute of Advanced Steels and Materials, School of Materials Science and Engineering, Shanghai Jiao Tong University, Shanghai 200240, China. LI WANG, Chief Engineer, and SHU ZHOU, Junior Engineer, are with the State Key Lab of Development and Application Technology of Automotive Steels, Baosteel Research Institute, Shanghai 201900, China.
Manuscript submitted December 23, 2015.
Article published online June 14, 2016.

in ferrite, the microhardness of partitioned martensite, the load distribution between ferrite and martensite, and the volume fraction change of RA. A mechanical model was constructed based on Mecking–Kocks model, Bouquerel's spherical assumption, and Gladman-type mixture law. The hardening effect of secondary phase was simulated by this model, and verified by comparing with the experimental results of the bake-hardened specimen. This study is instrumental not only in understanding the deformation mechanism of multi-phase steels but also paving the way for enhancing mechanical properties via microstructural optimization.

II. EXPERIMENTAL PROCEDURES

A 1.6-mm-thick cold-rolled low-carbon steel sheet (supplied by Baosteel) composed of pearlite and ferrite is used as the starting material. The nominal chemical composition is Fe-0.2C-1.40Si-1.80Mn (in wt pct). Two types of heat treatments were carried out to obtain different morphologies and distributions of martensite phase. For S-QP820 treatment (provided by Baosteel), samples were held at 1133 K (860 °C) for 5 minutes, slowly cooled to intercritical temperatures 1093 K ± 20 K (820 °C ± 20 °C), and quenched in a 573 K (300 °C) salt bath for 10 seconds, reheated and held at a partitioning temperature of 723 K (450 °C) for 30 seconds, and quenched again to room temperature. The slow cooling was deliberately designed to allow the formation of pro-eutectoid ferrite as well as a non-uniform carbon distribution in the RA. For I-QP treatment, samples were oil quenched to produce martensite microstructure after austenitizing at 1133 K (860 °C) for 5 minutes. These samples were then held at different intercritical temperatures for 5 minutes, then quenched and partitioned the same as S-QP samples. We conducted a series of I-QP experiments in the lab and found that the volume fractions of each phase in S-QP820 and I-QP820 [intercritical temperature 1093 K (820 °C)] are identical. The mechanical property optimized sample is I-QP800 (intercritical temperature 1073 K, i.e., 800 °C). In addition, a bake-hardened S-QP820 specimen which was pre-strained by 2 pct and tempered at 453 K (180 °C) for 2 hours in salt bath was prepared to study the hardening effect of secondary phase.

Tensile samples were tested by a Zwick universal testing machine (BTC-T1-FR020 TN.A50) with a strain rate of 0.5 mm/min at room temperature and the gage length was set to 25 mm (ASTM E 8M-04). The tensile axis was selected along the rolling direction. Interrupted tensile tests were performed at different engineering strains. Microhardness tests were performed on a Zwick/Roell microhardness tester with 10 gf load and 15 seconds dwell time. The distance between the indentations was 30 μm, which is three times larger than the indentation diagonal (about 7 μm) to avoid the interaction between the work hardening regions. The diagonal length of each indentation was scaled manually to reduce the experimental errors.

Microstructures were characterized by a two-step color-tint-etching method (4 pct picral solution and 10 pct aqueous solution of sodium metabisulfite).[27] These specimens were observed under an optical microscope equipped with a high-brightness halogen lamp (ZEISS AxidoCam MRC5). The samples for XRD (Ultima IV Rigaku), EBSD (AZTEC HKL), and TEM (JEOL 2100) were electrolytically or twin-jet polished with an electrolyte consisting of 5 pct perchloric acid and 95 pct glacial acetic acid at room temperature. The step size for EBSD was 100 nm. The volume fractions of RA at different strains were measured via saturation magnetization measurements[28] in a Quantum Design Physical Property Measurement System (PPMS-9T (EC-II)). The as-received Q&P specimen was annealed at 873 K (600 °C) for 1 hour to obtain the reference specimen free of austenite.

III. RESULTS AND DISCUSSION

A. Evolution of Microstructures

Representative optical microstructures of S-QP and I-QP specimens are shown in Figure 1. All samples consist of a martensite and ferrite matrix with certain content of dispersed RA. Color-tint-etching method has been proved an effective way to distinguish the three phases in our previous study.[27,29,30] Martensite and ferrite can be distinguished under the normal pattern, as shown in Figure 1(a). The sodium metabisulfite tinted the ferrite and martensite but not the austenite[31] which appears as the white phase in Figure 1(b). The volume fraction of each phase is measured by automatic areal analysis with an image analyzer on the color-tinted micrographs, as shown in Figure 2. The fraction of F/M and RA are corrected by the SEM micrographs and saturation magnetization measurement result, respectively.

The morphology and distribution of martensite are affected by the initial structure, nucleation, and growth of the new phase, which is similar to that reported for conventional DP steel,[19] and the SEM micrographs are shown in Figure 2. For the S-QP specimens, as shown in Figure 3(a), ferrite nucleates at the austenite grain boundary and grows into the austenite while cooling from austenitizing temperature to the intercritical temperature. Blocky martensite is the product of austenite transformation during quenching. For the I-QP specimens, the fine and uniform distributed martensite depends on the reversion of austenite from the initial martensite. A large number of different types of nucleation sites, such as prior austenitic boundaries, martensitic plate/lath boundaries, and carbide precipitates, are available in the martensite microstructure. But as reported in the literature,[19] martensite in QP samples is also coarse when the combined volume fraction of martensite and RA is about 50 pct, as shown in Figures 3(b) and (c).

B. Mechanical Properties and Deformation Analysis

Figure 4(a) shows the typical engineering stress–strain curves obtained by tensile tests on three groups of specimens. The mechanical properties and product of
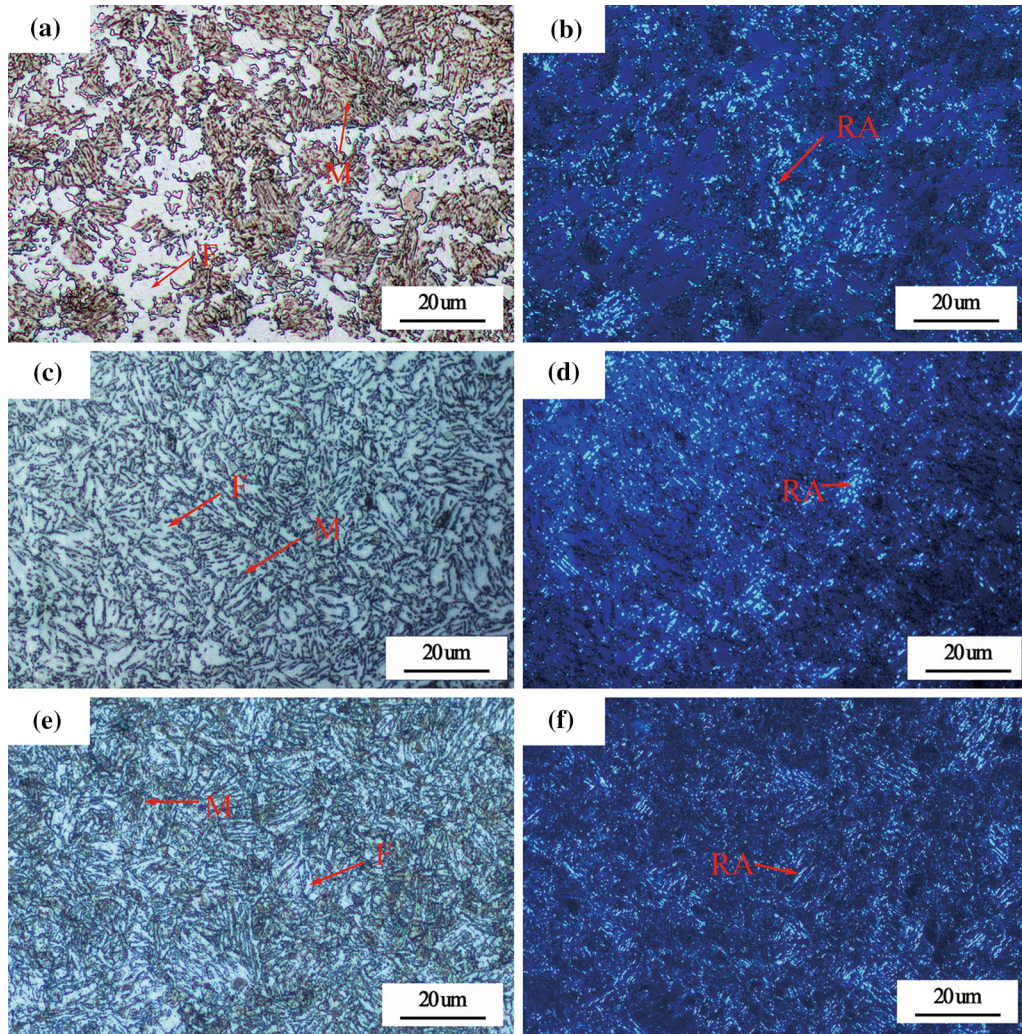
Fig. 1—Two-step color-tint-etching micrographs. (*a*), (*c*), (*e*) are micrographs obtained under normal pattern of S-QP820, I-QP800, I-QP820. (*b*), (*d*), (*f*) are identical microstructures taken under the polarized light.
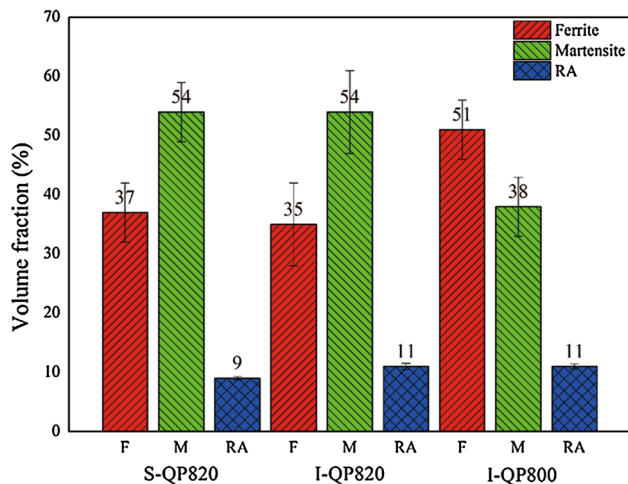

Fig. 2—Volume fraction of each phase of the three specimens.

uniform strain (ε_e) and total strain (ε_u) of I-QP800 specimen are much higher than those of S-QP820 and I-QP820 specimens. Although the morphology of I-QP820 specimen is a mixture of fine and blocky martensite, its mechanical property is close to S-QP820 specimen composed of blocky martensite. The difference in mechanical property should be related to the effect of morphology and distribution of martensite and the role of RA, which will be discussed in the next section.

The work hardening behavior of the stress–strain curve can be understood by the Crussard–Jaoul (C–J) analysis, which is useful in analyzing the multi-strain stage,[32] the steady-state stress,[33] and the intensity of internal stress.[34] The equations are expressed as

$$\sigma = \sigma_0 + k\varepsilon^n \qquad [1]$$

strength and elongation ($\sigma_u \times \varepsilon_u$) are listed in Table I. The yield strength (σ_0) of I-QP800 specimen is lower than that of S-QP820 and I-QP820 specimens, but the

$$\ln(d\sigma/d\varepsilon) = \ln(kn) + (n-1)\ln\varepsilon, \qquad [2]$$

where the slope of the $\ln(d\sigma/d\varepsilon) - \ln\varepsilon$ plot, yields ($n-1$). The calculated results are shown in Figure 4(b). The fitting parameters for different stages and strain
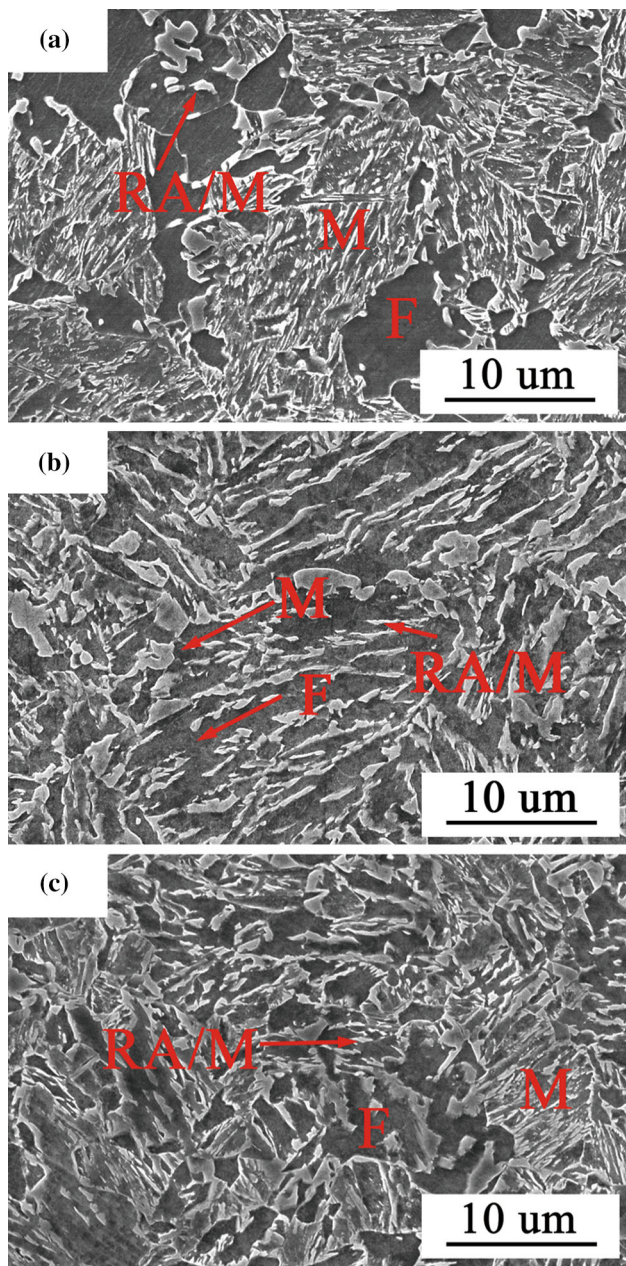
Fig. 3—The SEM micrographs of the three specimens. (*a*) S-QP820; (*b*) I-QP800; (*c*) I-QP820.

range of each stage for the three specimens are listed in Table II. The negative values of n and k are associated with a high internal stress field[34] or corresponding to deformation where dynamic recovery is dominant.[35] When n is negative, the equation can be rewritten as

$$\sigma = \sigma_0 - |k|/\varepsilon^{|n|}. \qquad [3]$$

In stage I, the negative values of work hardening index $n1$ for the three specimens is probably correlated to the increased dislocations as a result of the RA transformation.[29] As the calculated saturated stress σ_1 approaches the ultimate tensile strength σ_u, the homogeneity of dislocation distribution is affected by the martensite morphology (discussed in Section III–C) and further by the martensite plastic deformation (discussed in Section III–E).

The ranges of strain in Stages II and III are identical for all three specimens, so are the values of n. This implies that the deformation behaviors are similar for the specimens in the chosen strain ranges. Strain concentration is supposed to occur at Stage III, and this supposition is discussed in Section III–D by the evolution of observed dislocation density.

Stage IV is a unique feature found only in I-QP800 sample. The strength σ_4 is equal to 2649 MPa, which approaches the yield strength of martensite particles induced by the transformation of high-carbon RA. In addition, the work hardening index n_4 is a negative value, which is interpreted as the plastic deformation onset of harder particles and/or a high internal stress field in Reference 34.

The S-QP820 and I-QP800 specimens are selected to study the effect of the martensite morphology and distributions and the role of RA stability.

C. The Effect of the Martensite Morphology

The microstructure and local misorientation map of S-QP820 and I-QP800 are characterized by EBSD, and are shown in Figures 5 and 6, respectively. As shown in Figures 5(a) and (b), before tensile test the misorientation of the ferrite is less than 2 deg (blue regions with green dots). Most of the blue regions of I-QP800 specimen contain more green dots than S-QP820 specimen, but some blue regions with green/yellow band are found in S-QP820 specimen. This observation is confirmed in Figure 5(c), which shows the relative frequency distribution of the local misorientation below 2 deg. The peak and full width at half-maximum (FWHM) values are obtained by Gaussian peak fitting. The peak value can be assumed proportional to the mean dislocation density as discussed in Reference 36; the FWHM value can reflect the strain heterogeneity:[37] the higher the value of FWHM is, the more the strain is concentrated.

Comparing the band contrast map and the local misorientation map revealed significantly increased strain and heterogeneous strain distribution in the post-fracture S-QP820 specimen, especially in the ferrite phase, as shown in Figures 6(a) and (b). Strain concentrates in a quite large area, albeit relative low misorientation regions in ferrite still exist. As for the I-QP800 specimen, strain distributes homogeneously, as shown in Figures 6(c) and (d). The relative frequency distribution of local misorientation and the values of Gaussian fitting peaks and FWHM of the two specimens are shown in Figure 6(e). The FWHM value of S-QP820 is higher than that of I-QP800 specimen. S-QP820 specimen with coarse and blocky martensite produces larger strain concentration than I-QP820 specimen with fine and uniformly distributed martensite does, as the later specimen may relieve the inhomogeneous distribution of dislocations before tensile test and the load concentration in ferrite during tensile test.[38,39] The peak values of
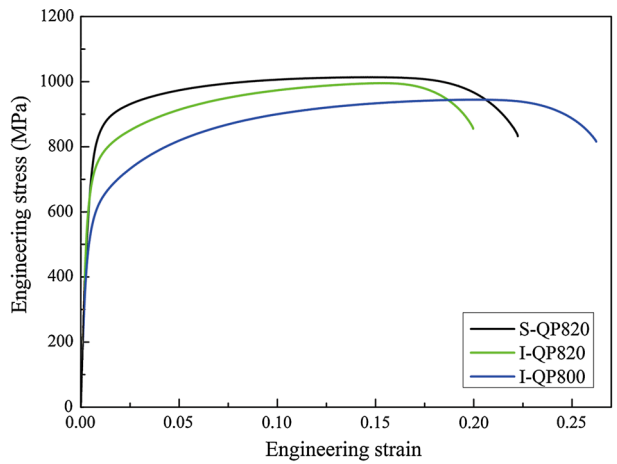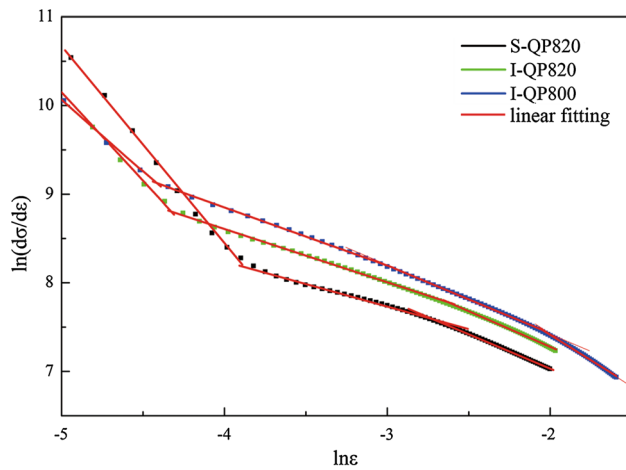
Fig. 4—(a) The engineering stress–strain curves. (b) The Crussard–Jaoul analyses of the tensile data (Color figure online).

both specimens are 0.65 even though the total elongations of the two specimens are different. This value is believed to be the saturation value of the dislocation density for ferrite. In addition, the unidentified proportion in I-QP800 is also higher than that in S-Q820, which implies larger plastic deformation or the existence of higher internal stress field. This result is consistent with the explanation of Stage IV by the $D_{C–J}$ analysis.

As shown in Figure 6, certain amount of RA remains at the low misorientation regions in S-QP820 specimen, while little RA remains in the fractured I-QP800 specimen. This is consistent with the tensile result that I-QP800 specimen has higher uniform and total elongation. The volume fraction of RA at different strains of S-QP820 and I-QP800 are measured by saturation magnetization measurement. As shown in Figure 7(a), the transformed proportions (transformed RA pct/initial RA pct) of S-QP820 and I-QP800 are about 60 and 87 pct, respectively. The stability of RA is estimated by the Olson–Cohen (OC) model with the following equation:[40]

$$f_{M}/f_{A0} = 1 - \exp\left(-B\left(1 - \exp\left(-A\varepsilon\right)\right)^2\right), \quad [4]$$

where f_{M} and f_{A0} are the volume fractions of induced martensite and initial RA, and A and B are fitting parameters. The carbon contents of RA of the two specimens are estimated from the lattice parameter α_0 measured by XRD,[41] and the average values for S-QP820 and I-QP800 are about 1.16 and 1.13 pct, respectively. As can be seen in Figure 7(b), the proportions of the induced martensite in both specimens are similar until Stage III. The difference after this stage is assumed to be caused by the difference in local strain concentration for the two specimens. For S-QP820 specimen, the RA located in the severely concentrated strain regions transforms too early to provide local

Table I. The List of Mechanical Properties and Product of Strength and Elongation

	σ_0 (MPa)	σ_u (MPa)	ε_e (Pct)	ε_u (Pct)	$\sigma_u \times \varepsilon_u$ (GPa Pct)
S-QP820	776 ± 40	1014 ± 5	14.5 ± 0.7	22.2 ± 1.6	22.5
I-QP820	732 ± 42	995 ± 3	15.1 ± 0.5	20.0 ± 2.1	19.9
I-QP800	532 ± 25	944 ± 3	19.9 ± 0.5	26.2 ± 1.8	24.7

Table II. The Crussard–Jaoul Fitting Parameters and Strain Range of Each Stage

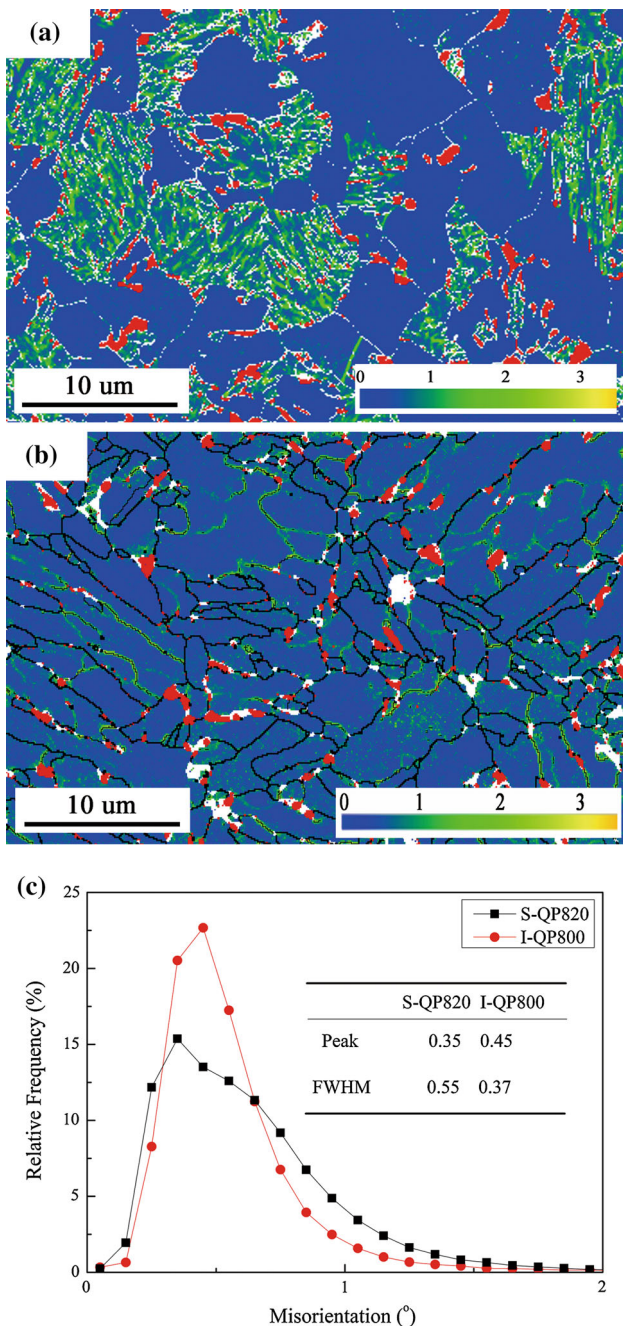|	I			II			III			IV		
	σ_1	k_1	n_1	σ_2	k_2	n_2	σ_3	k_3	n_3	σ_4	k_4	n_4
S-QP820	1001	−0.47	−1.24	792	1036	0.50	390	1174	0.21	—	—	—
Strain*	0.006–0.022			0.022–0.063			0.063–0.135			—		
I-QP820	894	−1.21	−0.99	588	1246	0.40	319	1323	0.24	—	—	—
Strain	0.006–0.013			0.013–0.068			0.068–0.140			—		
I-QP800	831	−11	−0.62	330	1479	0.34	125	1521	0.24	2649	−1195	−0.14
Strain	0.006–0.012			0.012–0.052			0.052–0.130			0.130–0.180		

* True strain.

(a)

10 um

(b)

10 um

(c)

Fig. 5—Local misorientation map plus RA phase of S-QP820 and I-QP800 specimens before tension, white represents non-indexed area, red represents FCC phase map. (*a*) S-QP820; (*b*) I-QP800. (*c*) the relative frequency distribution of the local misorientation below 2 deg (Color figure online).

strengthening that prevents local softening-induced necking upon further deformation. In contrast, RA in I-QP800 specimen is consumed equably due to the uniformly distributed martensite. The uniform and plentiful transformation occurred at high strain sustains the deformation of the matrix to the next stage.

D. The Dislocation Density Analysis of Ferrite

The properties of the constituent phase and phase interaction are needed for the mechanical modeling. In order to obtain an accurate description of martensite, S-QP820 specimen containing blocky martensite is selected for the following research.

Firstly, the dislocation evolution is characterized by TEM using two beam contrast condition. As can be seen in Figure 8, randomly distributed straight dislocations are the primary structure before tension in Figure 8(a). Irregular tangles are the dominant structure at 5 pct strain as shown in Figure 8(b). At 11 pct strain, incipient cell structures are observed in Figure 8(c). A well-developed cell structure is predominant in the ferrite at 14 pct strain as shown in Figure 8(d). It is assumed that local strain concentration occurs in this stage according to the cell structure formation. Besides, in our previous study,[29] certain amount of RA is located inside the ferrite phase and responsible for the delayed dislocation cell formation in S-QP820 specimen compared with the dislocation evolution in DP steel studied by Korzekwa et al.[32] This hypothesis is further discussed in the following paragraph.

The dislocation density is calculated by the line intersection method according to Pešička et al.[42] The average values obtained from at least 10 different areas are plotted in Figure 9. The relationship between dislocation density and the strain can be modeled by Mecking–Kocks theory:

$$\frac{d\rho}{Md\varepsilon} = \frac{1}{bd} + \frac{k}{b}\sqrt{\rho} - f\rho, \qquad [5]$$

where $M = 3$ is the Taylor factor, b is the Burgers vector and is equal to 2.48×10^{-10} m for bcc structure, d is the grain size and is about 20 μm by the linear intercept technique,[43] and k and f are fitting parameters related to the production rate of required geometrical necessary dislocations and annihilation rate of dislocations, respectively. By fitting the model to experimental data, the obtained parameters are $k = 0.033$, $f = 7.5$. These values are different from those of polygonal ferrite ($k = 0.021, f = 6.27, \rho_0 \approx 10^{12}$)[44] but similar to the ones of bainitic ferrite ($k = 0.031$, $f = 7.64$, $\rho_0 \approx 10^{13}$ m^{-2}).[44] So the ferrite in S-QP820 specimen deforms in the same manner as bainitic ferrite due to the role of RA located inside the ferrite.

E. The Study of the Hardness of Individual Phase and Load Partitioning

Hardness test is an efficient tool for detecting small-scale mechanical properties and separating the active strengthening mechanisms in multiphase steels.[45,46] Three types of specific zones composed of an unequal or equal mixture of ferrite and martensite are selected for the microhardness tests. These zones are marked by four large indentations and a total of eight areas have been checked. One of the typical images is shown in Figure 10(a), where a series of indentations are tested and shown in Figure 10(b). A coordinate system is built at the center of the marked indentation; the relative coordinates of each center of the tested indentations are measured and transferred to the color-tint micrograph. Squares with a diagonal length of 7 μm,
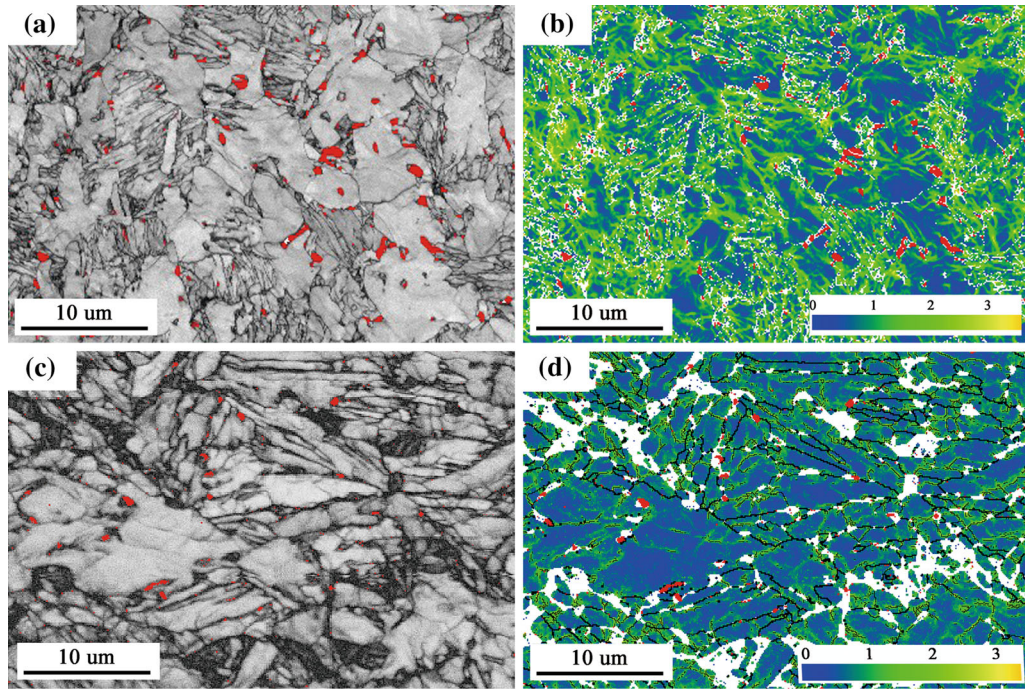
Fig. 6—The band contrast map and local misorientation map plus RA phase of S-QP820 and I-QP800 specimens after tension. (*a*) and (*b*) are micrographs of S-QP820; (*c*) and (*d*) are micrographs of I-QP800. (*e*) The relative frequency distribution of the local misorientation below 2 deg (Color figure online).

which mimic the hardness indentations, are superposed on this image. Using the digital image processing proposed in the previous study,[27] the three phases are differentiated by different colors. The content of each phase is calculated.

Ferrite and martensite have hardness values of 240 ± 13 and 400 ± 16 HV, respectively. The microhardness value of ferrite is comparable to the nanohardness value of ferrite in a similar dual-phase steels measured by Delince *et al.*[45] (~2.5 GPa according to Eq. [4]), but the value of martensite (~4 GPa) is smaller than theirs (~5.5 GPa). The discrepancy may arise from the fact that the hardness of martensite is not the hardness of the martensite block/lath, but rather the value of the packet property of martensite. Besides, the partitioning of carbon atoms may contribute to the difference. Since the carbon content of the martensite is conserved and equal to the carbon content of the austenite (c_A) in the intercritical temperature, its value

before and after partition (c_M) can be calculated by the mass balance below:

$$c_{total} = f_F c_F + f_A c_A \quad [6]$$

$$c_{total} = f_M c_M + f_{RA} c_{RA} + f_F c_F \quad [7]$$

given the values of $f_M = 0.54$, $f_{RA} = 0.09$, $f_F = 0.37$, $f_A = 0.63$, $c_{total} = 0.2$ pct, $c_{RA} = 1.16$ pct, $c_F = 0$, we obtain $c_A = 0.32$ pct and $c_M = 0.18$ pct, respectively. Therefore, considerable amount of carbon spreads out from the martensite during the partitioning treatment.

The load partitioning between ferrite and martensite is estimated below:

Firstly, the hardness value Hv(i), volume fractions of ferrite $f_F(i)$, and martensite $f_M(i)$ in the square are obtained in the example shown in Figure 10(a). Then the load partitioning between ferrite and martensite is supposed to bear the following relationship:
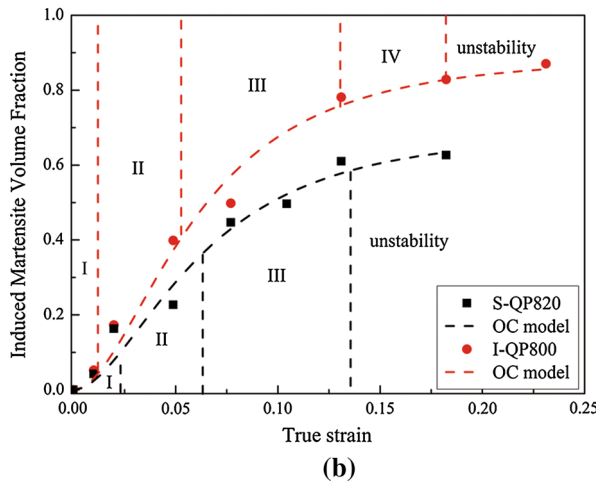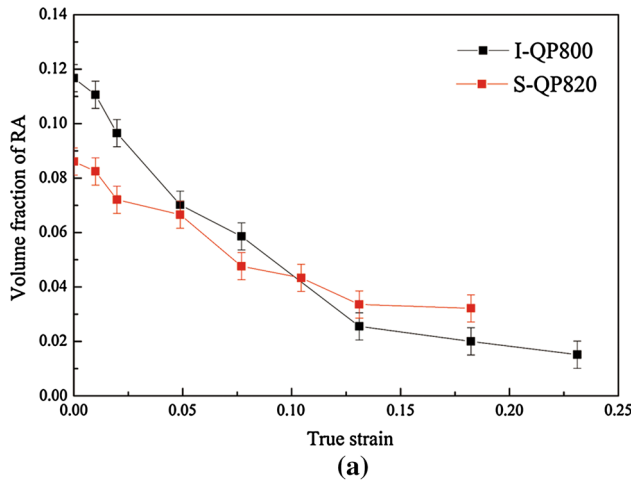
(a)

(b)

Fig. 7—(a) The volume fraction of RA of S-QP820 and I-QP800 specimens at different strain obtained by saturation magnetization measurement. (b) The stability of RA estimated by the Olson–Cohen model (Color figure online).

$$f'_F Hv_F + f'_M x Hv_M = Hv', \qquad [8]$$

where Hv_F and Hv_M are the hardness of ferrite and martensite, and take values of 240 and 400, respectively; Hv' is the given hardness value; f'_F and f'_M are the calculated volume fractions of ferrite and martensite for the given Hv'; and x is the weighting factor. Assuming $Hv' = Hv(i)$ and $f'_F = f_F(i)$, so one can calculate the volume fraction of martensite $x f'_M$. As shown in Figure 11, $x f'_M$ is linearly dependent on the measured results $f_M(i)$, which means the load partitioning of the two phases is according to the linear law ($x = 1$). This result is consistent with Reference 9 (the microhardness ratio between martensite (400 Hv) and ferrite (240 Hv) is about 1.6) and implies that the martensite may deform plastically after the yielding point due to the carbon depletion.

F. The Mechanical Modeling of S-QP820

The stress–strain curve of S-QP820 specimen is simulated in this section. The properties of the constituent phase are determined by the above experimental results or the theory and empirical equations.

The expected yield stress of ferrite is calculated from Pickerings equation:[47]

$$\sigma_0 = 77 + 32Mn + 83Si + 5544(N_{ss} + C_{ss}) + k_y d^{-\frac{1}{2}} + \alpha M G b \sqrt{\rho_0}, \qquad [9]$$

where the following constants are used in the work: Mn = 1.8 pct, Si = 1.4 pct, C_{ss} = 0.02 pct, k_y = 18 MPa $mm^{0.5}$, d = 20 $\times 10^{-3} mm^{0.5}$, α = 0.4, M = 3 (Taylor factor), G = 78,500 MPa (shear modulus for bcc), b = 2.48 $\times 10^{-10}$ m (Burgers vector in bcc iron),[44] and ρ_0 = 1.07 $\times 10^{14}$ m^{-2}. The yield strength of ferrite is about 730 MPa, which is in agreement with the measured value.

The mechanical behavior of ferrite is modeled by the Mecking–Kocks model:

$$\sigma = \sigma_0 + \alpha M G b \sqrt{\rho}, \qquad [10]$$

where the dislocation density has been measured and fitted in Section III–E.

The load distribution between ferrite and martensite was assumed to be the same and has been verified by the hardness test. The mechanical property follows the Hollomon type of power law given by

$$\sigma_M = K_M \varepsilon^{n_M}, \qquad [11]$$

where the parameters of martensite in this steel are taken as K_M = 1496 MPa and n_M = 0.08 by referring to a similar metastable RA containing dual-phase steel.[48]

The spherical assumption proposed by Bouquerel et al.[44] is used to model the behavior of the RA/M' constituent during deformation. The strain-dependent grain size for the RA is described by

$$d_{RA}(\varepsilon) = d_{RAinit} \sqrt[3]{1 - f_{M'}}, \qquad [12]$$

where d_{RAinit} is the initial grain size of the RA. $f_{M'}$ is the volume fraction of induced martensite, and has been calculated by the Olson–Cohen model in Section III–C.

The stress–strain curves of RA is also modeled by Mecking–Kocks law, but the mean free path d is assumed to be equal to d_{RAinit}, and Eq. [5] then becomes

$$\frac{d\rho}{Md\varepsilon} = \frac{1}{b}\left(\frac{1}{d_{RAinit}\sqrt[3]{1 - f_{M'}}} + k\sqrt{\rho}\right) - f\rho. \qquad [13]$$

The yield strength of RA is 800 MPa according to the high carbon content.[2]

The stress–strain curve of induced martensite is well described by

$$\sigma - \sigma_0 = \Delta\sigma = \alpha\mu M\sqrt{b}\sqrt{\frac{1 - \exp(-Mf\varepsilon)}{fL}}, \qquad [14]$$

where L is the martensite size and is equal to $(\pi/6)d_{RAinit}^3$. The yield strength of martensite is determined as follows:
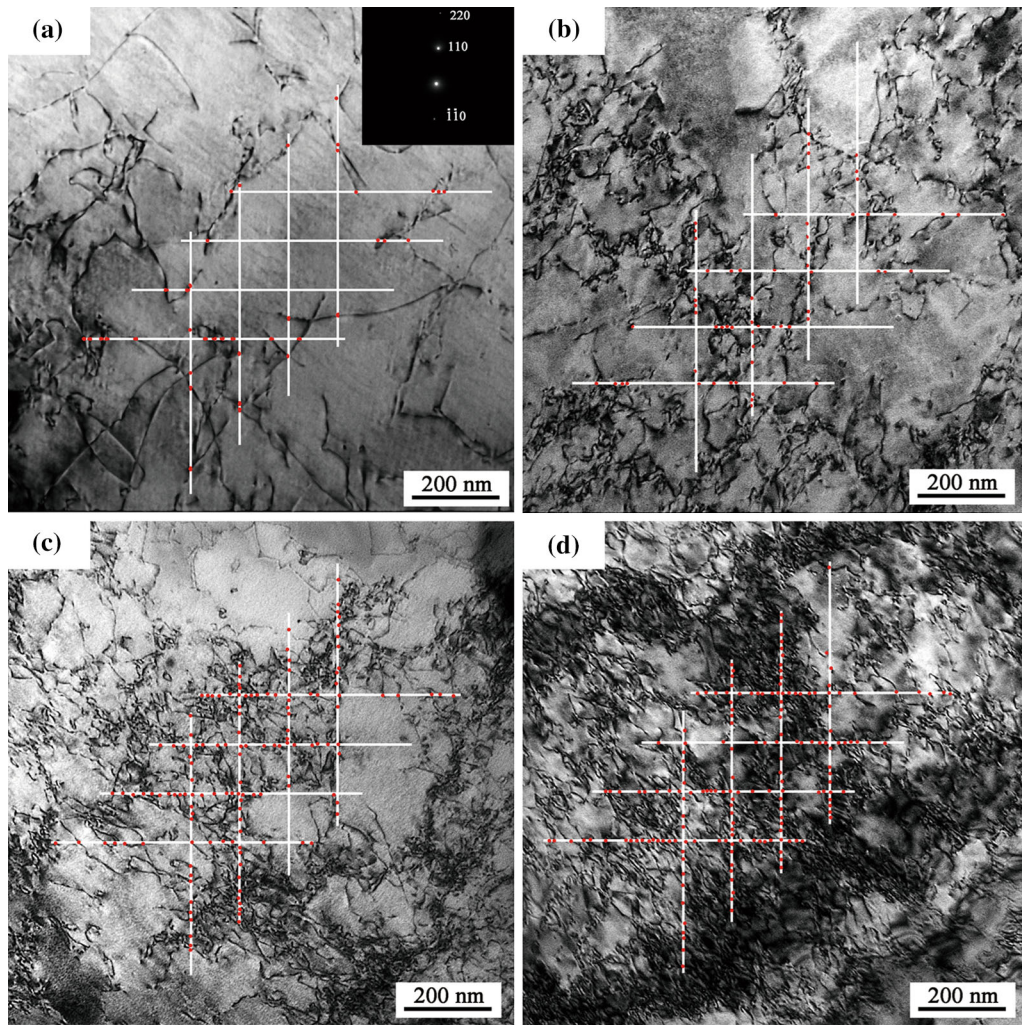
Fig. 8—Typical TEM micrographs of the dislocations in ferrite of S-QP820 specimen at different strains, (*a*) original specimen; (*b*) at 5 pct strain; (*c*) at 11 pct strain; (*d*) at 14 pct strain. The lines and intersections are inserted in the micrographs. Diffraction patterns are shown in the inset on the upper right in (*a*).
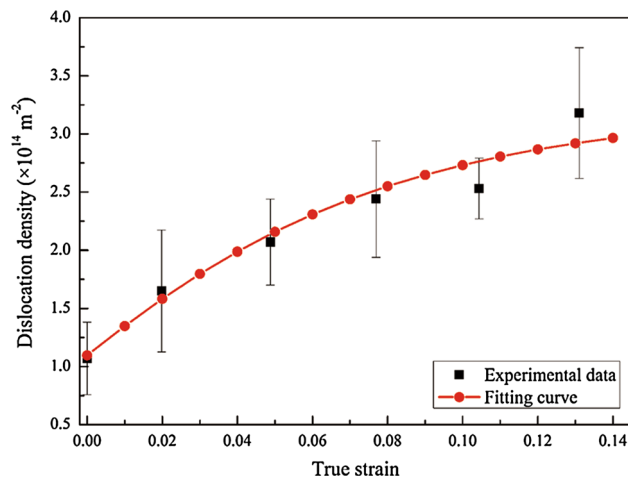

Fig. 9—Dislocation density at different strains measured by TEM and the fitting curve of S-QP820 specimen.

$$\sigma_{sM'}(\text{MPa}) = 413 + 1.72 \times 10^3 (\text{wt pct}C)^{1/2}, \quad [15]$$

where the carbon content of RA is about 1.16 pct, so $\sigma_{sM'} = 2266$ MPa.

The Gladman-type mixture law is used to describe the stress and strain curve of the steel:

$$\sigma_{AB} = \sigma_A\left(1 - f_A^n\right) + \sigma_B f_B^n, \quad [16]$$

where *n* is determined by the fitting.

The input parameters for this steel are reported in Table III, and the fitting result of each phase and the final model curve are plotted in Figure 12. An excellent match is obtained between the experimental results and the model calculations. When the volume fraction of RA is about 10 pct, the transformed proportion is about 60 pct, but the induced strength increment is only about 50 MPa. So the mechanical property is mainly determined by the matrix phases. The primary function of
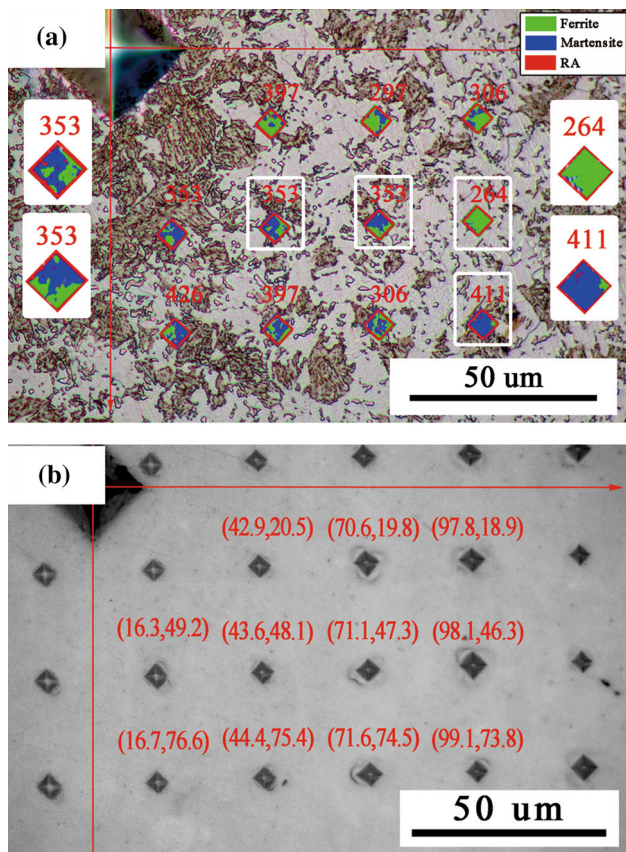
Fig. 10—Two-step color-tint-etching micrographs and the indentation results. (a) Color-tint-etching micrographs, the numbers above the square are the hardness values. (b) The indentation and the coordinate values.

RA is to maintain the deformation of the matrix phase by preventing local softening-induced necking. However, when the volume fraction of austenite is increased to about 30 pct, like the situation in medium manganese steels,[22] the 60 pct transformation of induced martensite can provide about 160 MPa added strength for this type of steel.

G. The Analysis of Bake-Hardened Specimen

Bake-hardened S-QP820 specimen is designed to study the role of secondary phase strengthening. Bake hardening is essentially a strain aging process involving interactions between interstitial atoms and dislocations,[49–51] which improves the yield strength and RA stability. The pre-straining is selected to be 2 pct because most of the RA located inside the ferrite is transformed before 2 pct according to our previous study.[29]

The tensile curve of the pre-staining and bake-hardened specimen as well as the volume fractions of RA at different strains measured by saturation magnetization measurement are shown in Figure 13. The stress–strain curve consists of two platforms. The strength of the first and second platforms is about 1010 and 1025 MPa, respectively. Compared with the change in RA, the
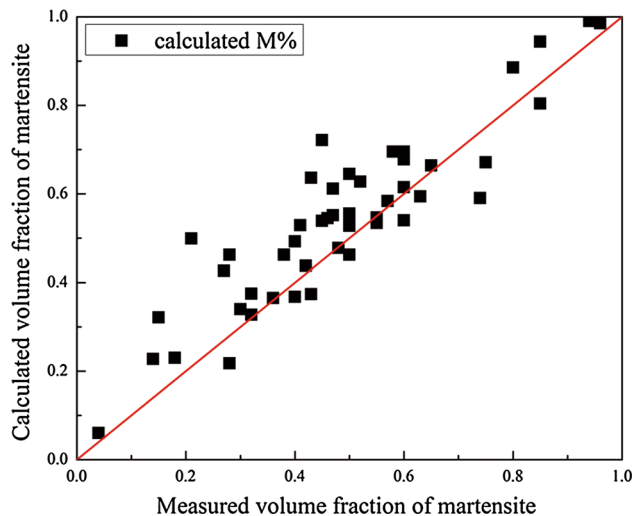

Fig. 11—Comparison of the measured and calculated volume fraction of martensite.

strength difference (about 15 MPa) between the two platforms is attributed to the existence of the induced martensite (about 2.5 pct RA transformed to martensite). According to the stress–strain model used in Section III–F, when the initial volume fraction of RA is about 6.4 pct and the transformed proportion is about 40 pct (about equal to 2.5 pct), the strength increment caused by the induced martensite is about 19 MPa, consistent with the experimental result. The bake-hardened specimen effectively verifies the function of secondary phase strengthening. More work is in progress to elucidate the complex but interesting phenomenon existed in the bake-hardened specimen.

IV. CONCLUSIONS

In this paper, the deformation behavior is studied by analyzing the phase interaction and the TRIP effect in two different types of multiphase steels containing quenching and partitioning-treated martensite. The mechanical behavior is modeled based on the Mecking–Kocks theory, Bouquerel's spherical assumption and the Gladman-type mixture law. The main conclusions are summarized as follows:

1. The product of strength and elongation of I-QP800 specimen containing fine and uniformly distributed martensite is higher than that of S-QP820 specimen with blocky martensite. The martensite in QP820 specimen is coarse when its volume fraction is about 50 pct, and this specimen performs the same as S-QP820 specimen.
2. Martensite morphology and distribution affect the strain distribution, and subsequently affect the function of RA. As for the S-QP820 specimen, RA located in the strain-concentrated region transforms too early to prevent the local failure in high strain. In contrast, plentiful RA in I-QP800

Table III. Input Parameters for the Stress–Strain Curves of S-QP820 Specimen

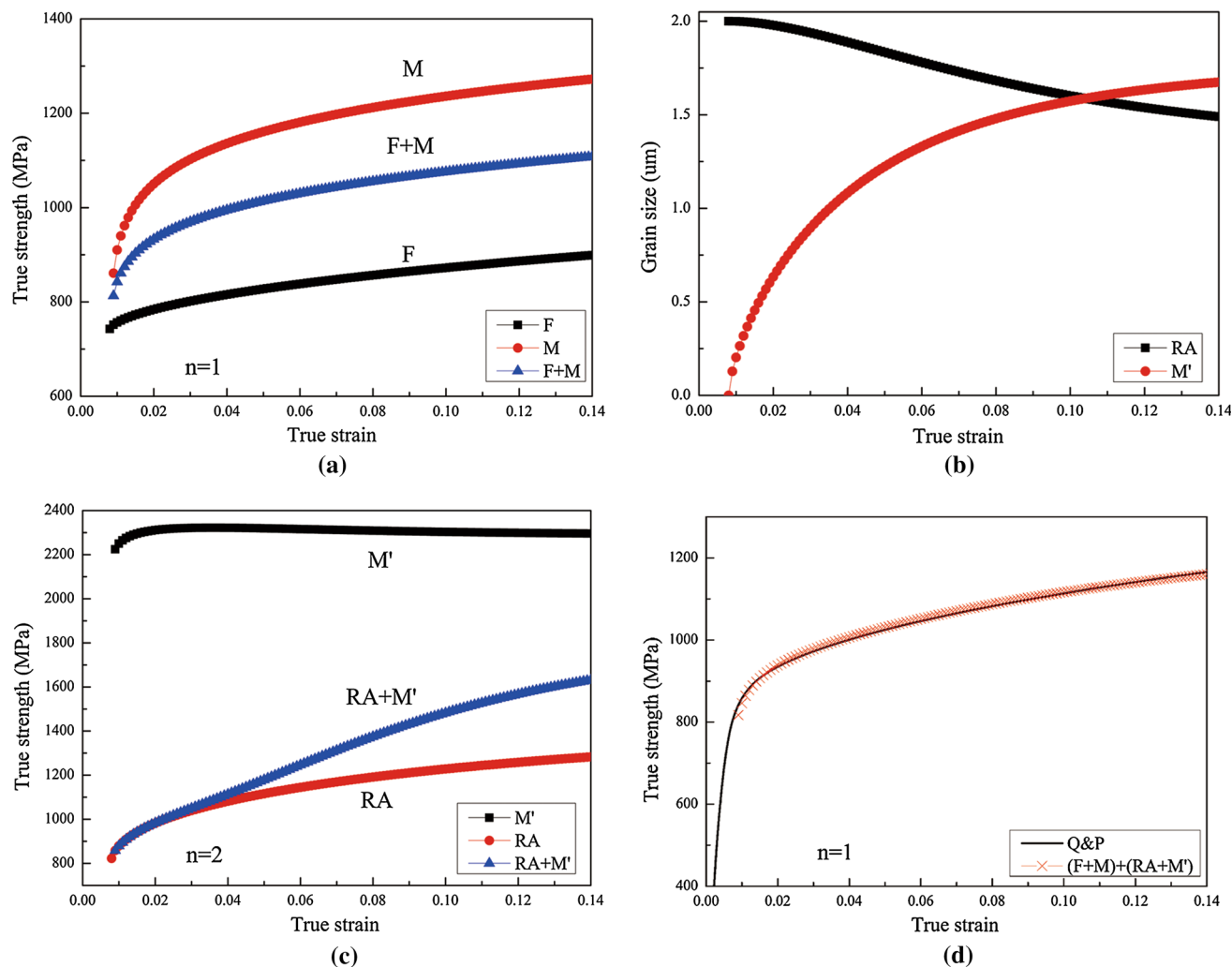|	F	M	RA	M′
Stress–Strain	Eqs. [5] and [10]	Eq. [11]	Eqs. [10] and [13]	Eq. [14]
Yield Strength (MPa)	Eq. [9]	Eq. [15]	800	Eq. [15]
Grain Size (μm)	20	—	2	$(\pi/6)d_{RAinit}^3$
k	0.033	—	0	0
f	7.5	—	4	15
n Mixture Law F/M	1			
n Mixture Law RA/M′	2			
n Mixture Law S-QP	1			

Fig. 12—(a) Estimated stress–strain curves of the M/F matrix phases. (b) Evolution of the estimated grain size for RA and transformation-induced martensite. (c) Estimated stress–strain curves for the RA/M′ constituent. (d) Stress–strain curves for the S-QP820 specimen.

specimen transforms uniformly at high strain, which efficiently sustains the deformation of the matrix phases.

3. The strain concentration may occur late in Stage III according to the D_{C-J} analysis and the dislocation evolution. Ferrite in the S-QP820 specimen is found to deform the same as that in bainitic ferrite does.

4. A coordinate conversion method is proposed to investigate the relationship between microhardness and

microstructure of multiphase steels. The partitioned martensite is alike tempered martensite to some extent. The load partitioning between ferrite and partitioned martensite conforms to the linear mixture law.

5. According to the mechanical model, the property is mainly determined by the property of the matrix phases. The secondary phase strengthening effect is dependent on the initial volume fraction of RA and the transformed proportions.
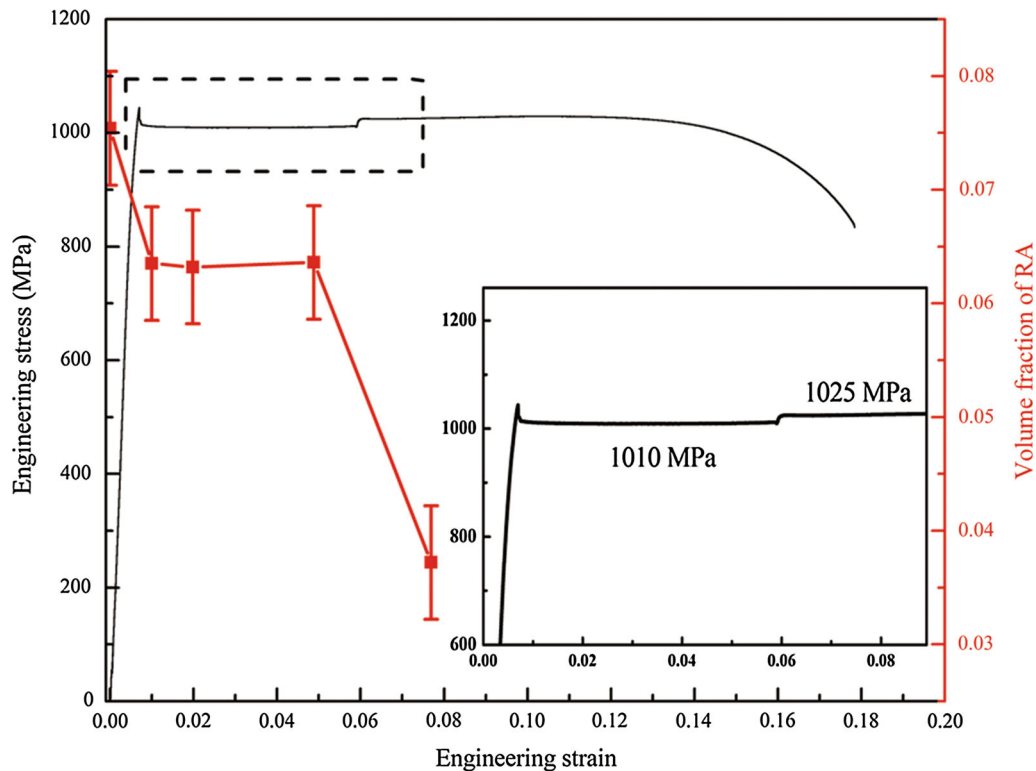
Fig. 13—The stress–strain curve and volume fraction of RA of pre-straining and bake-hardening-treated S-QP820 specimen.

6. The different strength at the platform of the stress–strain curves of bake-hardened S-QP820 specimens is attributed to the existence of transformation-induced martensite. The increased value is consistent with the value predicted by the model.

REFERENCES

1. D.K. Matlock and J.G. Speer: *In Microstructure and Texture in Steels*, Springer, Berlin, 2009, pp. 185–205.
2. B. Fu, W. Yang, Y. Wang, L. Li, Z. Sun, and Y. Ren: *Acta Mater.*, 2014, vol. 76, pp. 342–54.
3. P.J. Jacques, Q. Furnémont, F. Lani, T. Pardoen, and F. Delannay: *Acta Mater.*, 2007, vol. 55, pp. 3681–93.
4. J. Speer, D.K. Matlock, B.C. De Cooman, and J.G. Schroth: *Acta Mater.*, 2003, vol. 51, pp. 2611–22.
5. A.J. Clarke, J.G. Speer, D.K. Matlock, F.C. Rizzo, D.V. Edmonds, and M.J. Santofimia: *Scripta Mater.*, 2009, vol. 61, pp. 149–52.
6. M.J. Santofimia, L. Zhao, R. Petrov, and J. Sietsma: *Mater. Charact.*, 2008, vol. 59, pp. 1758–64.
7. E. De Moor, S. Lacroix, A. Clarke, J. Penning, and J. Speer: *Metall. Mater. Trans. A*, 2008, vol. 39A, pp. 2586–95.
8. J. Kang, Y. Ososkov, J.D. Embury, and D.S. Wilkinson: *Scripta Mater.*, 2007, vol. 56, pp. 999–1002.
9. H. Shen, T. Lei, and J. Liu: *Mater. Sci. Technol.*, 1986, vol. 2, pp. 28–33.
10. M. Mazinani and W. Poole: *Metall. Mater. Trans. A*, 2007, vol. 38A, pp. 328–39.
11. Y. Su and J. Gurland: *Mater. Sci. Eng.*, 1987, vol. 95, pp. 151–65.
12. A. Rizk and D. Bourell: *Scripta Metall.*, 1982, vol. 16, pp. 1321–24.
13. Y. Tomota, K. Kuroki, T. Mori, and I. Tamura: *Mater. Sci. Eng.*, 1976, vol. 24, pp. 85–94.
14. S. Mileiko: *J. Mater. Sci.*, 1969, vol. 4, pp. 974–77.
15. Z. Jiang, Z. Guan, and J. Lian: *Mat. Sci. Eng. A*, 1995, vol. 190, pp. 55–64.
16. R. Davies: *Metall. Mater. Trans. A*, 1978, vol. 9A, pp. 451–55.
17. R. Davies: *Metall. Mater. Trans. A*, 1978, vol. 9A, pp. 671–9.
18. R. Grange, C. Hribal, and L. Porter: *Metall. Trans. A*, 1977, vol. 8, pp. 1775–85.
19. A. Bag, K. Ray, and E. Dwarakadasa: *Metall. Mater. Trans. A*, 1999, vol. 30A, pp. 1193–1202.
20. N.C. Goel, S. Sangal, and K. Tangri: *Metall. Trans. A*, 1985, vol. 16A, pp. 2013–21.
21. Y. Tomota, H. Tokuda, Y. Adachi, M. Wakita, N. Minakawa, A. Moriai, and Y. Morii: *Acta Mater.*, 2004, vol. 52, pp. 5737–45.
22. J. Shi, X. Sun, M. Wang, W. Hui, H. Dong, and W. Cao: *Scripta Mater.*, 2010, vol. 63, pp. 815–18.
23. C. Kim: *Metall. Trans. A*, 1988, vol. 19, pp. 1263–8.
24. D. Bourell and A. Rizk: *Acta Metall.*, 1983, vol. 31, pp. 609–17.
25. P. Jacques: *Curr. Opin. Solid. St. M.*, 2004, vol. 8, pp. 259–65.
26. R.J. Moat, S.Y. Zhang, J. Kelleher, A.F. Mark, T. Mori, and P.J. Withers: *Acta Mater.*, 2012, vol. 60, pp. 6931–39.
27. H.S. Zhao, X. Zhu, W. Li, X.J. Jin, L. Wang, H. Jiao, and D.M. Jiang: *Mater. Sci. Technol.*, 2014, vol. 30, pp. 1008–13.
28. L. Zhao, N. Van Dijk, E. Brück, J. Sietsma, and S. Van der Zwaag: *Mat. Sci. Eng. A*, 2001, vol. 313, pp. 145–52.
29. H. Zhao, W. Li, X. Zhu, X. Lu, L. Wang, S. Zhou, and X. Jin: *Mat. Sci. Eng. A*, 2016, vol. 649, pp. 18–26.

30. H. Zhao, W. Li, X. Zhu, X. Lu, L. Wang, S. Zhou and X. Jin: *Mater. Sci. Technol.* 2016, pp. 1–6.
31. A.K. De, J.G. Speer, and D.K. Matlock: *Adv. Mater. Processes*, 2003, vol. 161, pp. 27–30.
32. D. Korzekwa, D. Matlock, and G. Krauss: *Metall. Trans. A*, 1984, vol. 15A, pp. 1221–8.
33. S. Sankaran, S. Sangal, and K. Padmanabhan: *Mater. Sci. Technol.*, 2005, vol. 21, pp. 1152–60.
34. M. Umemoto, K. Tsuchiya, Z. Liu, and S. Sugimoto: *Metall. Mater. Trans. A*, 2000, vol. 31A, pp. 1785–94.
35. D. Das and P.P. Chattopadhyay: *J. Mater. Sci.*, 2009, vol. 44, pp. 2957–65.
36. M. Calcagnotto, D. Ponge, E. Demir, and D. Raabe: *Mat. Sci. Eng. A*, 2010, vol. 527, pp. 2738–46.
37. F. Maresca, V. Kouznetsova, and M. Geers: *Scripta Mater.*, 2016, vol. 110, pp. 74–77.
38. N. Kim and G. Thomas: *Metall. Trans. A*, 1981, vol. 12A, pp. 483–9.
39. S. Kim and S. Lee: *Metall. Mater. Trans. A*, 2000, vol. 31A, pp. 1753–60.
40. G. Olson and M. Cohen: *Metall. Trans. A*, 1975, vol. 6A, pp. 791–5.
41. S.-J. Lee, J. Mola, and B.C. De Cooman: *Metall. Mater. Trans. A*, 2012, vol. 43A, pp. 4921–5.
42. J. Pešička, R. Kužel, A. Dronhofer, and G. Eggeler: *Acta Mater.*, 2003, vol. 51, pp. 4847–62.
43. M.A. Meyers and K.K. Chawla: *Mechanical behavior of materials*, Cambridge University Press, Cambridge, 2009.
44. J. Bouquerel, K. Verbeken, and B. Decooman: *Acta Mater.*, 2006, vol. 54, pp. 1443–56.
45. M. Delince, P. Jacques, and T. Pardoen: *Acta Mater.*, 2006, vol. 54, pp. 3395–3404.
46. W. Horvath, W. Prantl, H. Stroißnigg, and E. Werner: *Mat. Sci. Eng. A*, 1998, vol. 256, pp. 227–36.
47. I. Gutiérrez and M.A. Altuna: *Acta Mater.*, 2008, vol. 56, pp. 4682–90.
48. S. Sangal, N.C. Goel, and K. Tangri: *Metall. Trans. A*, 1985, vol. 16A, pp. 2023–9.
49. A. De, K. De Blauwe, S. Vandeputte, and B. De Cooman: *J. Alloy. Compd.*, 2000, vol. 310, pp. 405–10.
50. S. Berbenni, V. Favier, X. Lemoine, and M. Berveiller: *Scripta Mater.*, 2004, vol. 51, pp. 303–8.
51. J. Zhao, A. De, and B. De Cooman: *Mater. Lett.*, 2000, vol. 44, pp. 374–8.